Fourth International Symposium on Marine Propulsors
SMP'15, Austin, Texas, USA, June 2015

Passive Vibration Control of Flexible Hydrofoils using Piezoelectric Material

Chenyang Li[1], Eun Jung Chae[2], Yin Lu Young[3]*, Xiaolin Wang[4], Silas Alben[5]

[1,2,3] Department. of Naval Architecture & Marine Engineering, The University of Michigan
[4,5] Department. of Mathematics, The University of Michigan
The University of Michigan at Ann Arbor, Ann Arbor, MI 48109, USA
* Corresponding author, ylyoung@umich.edu

ABSTRACT

This work explores the use of a piezoelectric material for passive vibration control of a cantilevered, flexible hydrofoil. The integrated fluid-solid-electrical response is modeled by coupling a 2-D viscous unsteady Reynolds Averaged Navier Stokes (uRANS) solver for the fluid with a two-degrees-of-freedom (2-DOF) solid model, which is coupled with the circuit equation. The two-way electro-mechanical coupling is assumed to be coupled to the foil bending degree of freedom only. PZT (lead zirconate titanate)-5H is selected due to its high electro-mechanical coupling factor, and the PZT beam is assumed to be bi-morphed. The results show that activation of the PZT circuit increases the vibration frequencies, as the electro-mechanical coupling force adds an additional stiffness term to the system stiffness. The changes on system stiffness and response frequency depend on the resistance. A well-tuned resistor in parallel with a PZT circuit can be used to delay flutter and control flow-induced vibrations.

Keywords

Passive vibration control, Flow-induced vibrations, PZT

1 INTRODUCTION

A rigid, but flexibly mounted, or a flexible hydrofoil, at an angle of attack will undergo flow-induced vibration if the center of pressure where the effective lift acts is away from the elastic axis, leading to deformations which will in turn interact with the flow. The focus of this work is to explore the use of PZT for passive flutter control. The critical flutter speed is defined when the total damping becomes zero; at speeds greater than the flutter speed, or post-flutter, the deformation will increase exponentially with time, which can lead to catastrophic failure if excessive deformation and/or accelerated fatigue leads to material failure.

Flow-induced vibrations are critical to many applications in marine and naval vessels. Compared to aerospace or wind energy harvesting structures, flow-induced vibrations in water can be more difficult to predict and control because of the directional dependence characteristic of fluid inertia, as well as the speed and frequency dependence of the fluid damping and disturbing forces. Viscous effects, cavitation, and free surface effects can further complicate the flow-induced vibrations.

As shown in previous analytical potential flow models developed by Theodorsen (1935), Sears (1941), and Garrick (1946), the flow-induced vibrations are related with the fluid inertial, damping, and disturbing forces. Recent works (Blake and Maga (1975); Chae et al (2013; 2015a,b)) have shown that classical potential theory can significantly over-predict the fluid damping in water for lightweight lifting bodies operating in heavy fluid, and hence predict a higher flutter/divergence speed than measured/observed. The results show that the flow-induced bend-twist coupling terms are highly dependent on viscous effects, and they affect the actual fluid damping and disturbing forces/moments, which cannot be predicted correctly with a linear potential flow solver (see Chae et al. (2015a,b) for more details). The over-prediction of the fluid damping creates a risk: structures may encounter earlier fatigue, increased noise and vibration, as well as earlier flutter and load amplification due to resonance or parametric excitation. Furthermore, the flow-induced vibrations can be generated by unsteady vortex shedding. The vortex shedding frequencies and wake patterns might interact with the foil deformations, and modify the fluid-structure interaction (FSI) responses and stability of the flexible hydrofoil. For example, when the vortex shedding frequency is near one of the natural frequencies of the flexible foil, the vortex shedding frequency will be modified and lock-in to the foil natural frequency, leading to low damping, long settling time, accelerated fatigue, and singing of propellers/hydrofoils (Chae et al., 2015a,b)). Therefore, accurate prediction and control of the flow-induced vibrations of flexible hydrofoils is needed to improve hydrodynamic/structural dynamic performance and ensure structural safety.

There are different ways to control flow-induced vibrations. Piezoelectricity is one of the topics which have been studied for use in sensing and controlling vibrations of flexible structures. Piezoelectric material is a type of active material (AMs) with two-way electro-mechanical conversion. The benefit of using AMs to control vibrations is that the AMs could be embedded within the structure without large change in structural mass or stiffness, and they could serve as both sensors and actuators. As one of the most widely used AMs, piezoelectric ceramics have high stiffness and high response frequency compared to other AMs (Monner, 2005), which makes them more suitable for vibration control.

There are two main methods of vibration control using piezoelectricity. The first one is active vibration control by changing the input voltage on piezoelectric ceramics attached to the structure. Active control methods for flexible beams have been discussed and experimentally tested by many, including Bailey and Ubbard (1985), Baz and Poh (1988), and Hagood et al. (1990). Although active control methods can be used to effectively reduce/cancel the vibrations, they are difficult to use for a wide variety of applications because they require a complex feedback control system that contains sensors, computer processors, amplifier, actuators and external electric sources. Moreover, addition of feed-back/feed-forward control algorithms may lead to new instabilities.

The second method is passive control method, which is the focus of this article. Compared to active control methods, passive control does not require a feedback control, which makes it simpler, cheaper and more reliable. However, the control authority of passive control methods can be limited and careful tailoring of the device is needed to ensure optimal performance in the full range of operating conditions. Passive control methods often require a shunting circuit (where a current divides into two or more paths before recombining to complete the circuit) to convert and dissipate vibration energy.

Much work has been done for controlling structural vibrations of cantilevered and clamped-clamped beams in air using the passive control method with a shutting circuit (see Hagood and von Flotow (1991); Wu (1996, 1998); Corr and Clark (2002) for examples). A passive piezoelectric control method by connecting a resistor and an inductor in series to piezoelectric patches was numerically derived for a cantilevered beam in air with bending degree of freedom only, and was experimentally validated to be effective to increase the damping for single mode of vibration (Hagood and von Flotow 1991). However, the required optimal inductor was found to be as large as 142H, which could be more than 250g in mass, and hence not feasible for most cases. Wu (1996) studied a shunting circuit connected in parallel to a resistor and an inductor to a piezoelectric patch that is attached to a cantilevered beam in air. He analytically derived the optimum values of resistance and inductance and validated the damping effect introduced by the piezoelectric circuit via numerical simulations and experiments. He then improved the shunting circuit by replacing the single resistor, inductor and capacitance in the circuit with multiple ones and successfully controlled multi-mode vibrations of a cantilevered beam in experiments conducted in air (Wu, 1998). A semi-active method introduced by Clark (2000) suggested that instead of changing electric parameters such as resistance in real time, switching the circuit states among open circuit and closed circuit of resistor and inductor shunt according to the electric input boundary may be more effective. In the experiment conducted in air shown in Corr and Clark (2002), the semi-active method allowed the optimal inductance to decrease from 10.5H to 0.5H. Recently, Schwarzendahl et al. (2012) expanded the PZT controlling concept from beams to blades by embedding a LR-Shunted PZT element (PZT element is connected to a shunting circuit with inductors and resistors) inside a cantilevered blade in air. By tuning the electric resonance to the mechanical resonance frequency, the resonant shunt causes the phase of the current to be shifted by approximately 90 degrees, and the resulting inverse piezoelectric effect will cause the LR-shunted PZT element to act as a tuned vibration energy absorber.

Though much work examined the structural damping effects induced by passive PZT control methods, only limited research considered FSI and viscous effects, which can drastically change the system dynamic response and stability. Doaré and Michelin (2011) derived a potential flow model coupled with the motion and circuit equations for a flexible plate embedded with bi-morphed piezoelectric patches immersed in the fluid domain subject to steady, uniform inflow. They found that the piezoelectric coupling coefficient and circuit response time to have significant influence on flutter boundaries of the flexible plate. However, their focus was for energy harvesting application only, not for vibration control.

The objective of this work is to numerically investigate the feasibility of passive flutter control of flexible foils in dense, viscous flow using a piezoelectric circuit with different resistance connected in parallel. The authors are also in the process of exploring the impact of adding an inductor in parallel and will show those results at the conference.

2 FORMULATION

A numerical model is used to investigate the flow-induced vibrations of a flexible hydrofoil and to explore passive vibration control using piezoelectric material. The

numerical model includes a structural model coupled with electro-mechanical model and a viscous flow solver.

2.1 Model Setup

The structure model of the simulation is a canonical, rectangular, cantilevered NACA16010 foil made of balsa wood with a chord length (c) of 0.3048 m and span length (S_p) of 1.2192 m placed in a freon/air mixture with fluid density (ρ_f) of 2.2 kg/m^3 and dynamic viscosity (μ_d) of 1.25×10^{-5} kg/(m·s). The problem setup is similar to that shown in Woolston and Castile (1951) where experimental measurements of the flutter speed and frequency of the cantilevered foil (without any PZT) inside a wind tunnel were reported. For simplicity, the foil is assumed to be chordwise rigid, while the spanwise bending (h) and twisting (θ) flexibilities are represented by translational and torsional springs with constants K_h and K_θ, respectively, placed at the elastic axis.

Inspired by the simple experimental piezo-aeroelastic system set up by Erturk et al. (2010), the free end of the cantilevered foil is assumed to be connected to a vertical rigid link element connected to a cantilevered PZT beam, as shown in Figure 1; the vertical deformation at the free end of the PZT beam is equal to bending deformation h of the foil. The rigid link element is placed at the elastic axis, which is very close to the aerodynamic center of the foil, and hence the PZT force is assumed to be coupled to the foil bending degree of freedom only for simplicity. A bi-morphed PZT configuration (continuous PZT patches on the top and bottom surfaces of the beam with a substrate layer in the middle) is assumed. The configuration and its equivalent circuit model are shown in Figure 2.

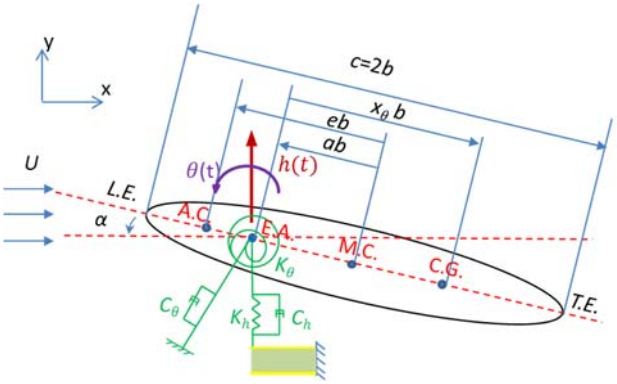

Figure 1: The model setup inspired by Erturk et al.'s experiment (2010), where the free end of a cantilevered airfoil is connected to a PZT beam by a vertical link element at the elastic axis (E.A.). L.E. and T.E. are the leading edge and trailing edge of the foil. A.C. is the aerodynamic center; M.C. is the mid-chord position; E.A. is the elastic axis; C.G. is the center of gravity. U is the inflow velocity; α is the angle of attack; $c = 2b$ is the chord length

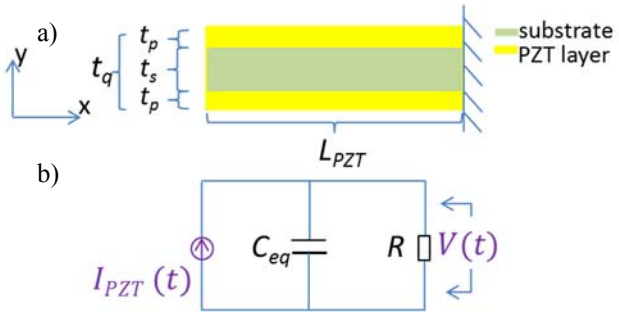

Figure 2: a) Bi-morphed PZT beam model. t_q is the total thickness; t_p, t_s are the thickness of PZT layers and substrate layer, respectively. L_{PZT} is the length of the PZT beam. b) Equivalent PZT circuit parallel connected with a resistor. R is the resistance, C_{eq} is the equivalent capacitance of the PZT material, I_{PZT} is the current generated by electro-mechanical conversion effect, V is the voltage on the PZT layers.

2.2 Governing Equations

The electro-mechanical model follows the formulation and experimental model used in Erturk and Inman (2009), where a bi-morphed piezoelectric beam is coupled with the heave deformation at the free end of a cantilevered foil.

The dimensional equation of motion (EOM) of the cantilevered hydrofoil is shown in Eq. (1).

$$\begin{aligned}&[M_s]\{\ddot{X}\}+[C_s]\{\dot{X}\}+[K_s]\{X\}\\&=\{F_{fluid}\}+\{F_{PZT}\}\end{aligned} \quad (1),$$

where $X = [\,h \quad \theta\,]^T$; h is the bending deformation at the free tip of the foil, defined positive upwards; and θ is the twisting deformation at the free tip of the foil, defined positive in the counter-clockwise direction about the E.A. at the free tip of the foil.

$$M_s=\begin{bmatrix} m & S_\theta \\ S_\theta & I_\theta \end{bmatrix}, C_s=\begin{bmatrix} C_h & 0 \\ 0 & C_\theta \end{bmatrix}, K_s=\begin{bmatrix} K_h & 0 \\ 0 & K_\theta \end{bmatrix} \quad (2),$$

M_s, C_s, and K_s are the dimensional structural mass, damping, stiffness matrices; m is the structural mass. $S_\theta = mx_\theta b$ is the static imbalance, where $x_\theta b$ is the distance from the E.A. to the C.G., defined positive towards the foil trailing edge. $I_\theta = mr_\theta^2 b^2$ is the structural moment of inertia defined about the elastic axis, where r_θ is the non-dimensional radius of gyration. $C_h = 2\zeta_{s,h} m\omega_h$ and $C_\theta = 2\zeta_{s,\theta} I_\theta \omega_\theta$ are the structural damping values for bending and twisting motions, respectively, where $\zeta_{s,h}$ and $\zeta_{s,\theta}$ are the corresponding non-dimensional damping coefficients; ω_h and ω_θ are the natural bending and twisting frequencies in vacuum. $K_h = m\omega_h^2$ and $K_\theta = I_\theta \omega_\theta^2$ are structural

bending and twisting stiffness. $F_{fluid} = [\ L_{fluid} \quad M_{fluid}\ ]^T$ is the flow induced force/moment calculated from a viscous flow solver (which will be explained later in this section), where L_{fluid} is the lift and M_{fluid} is the moment about E.A. defined positive in the counter-clockwise direction.

$F_{PZT} = [\ -V\beta_f/S_p \quad 0\ ]^T$ is the PZT induced force/moment, and is coupled to the foil's bending degree of freedom through the electro-mechanical coupling coefficient β_f shown on the right hand side of Eq. (3); V is the voltage and S_p is the span length. The circuit equation, Eq. (3), is the same as the circuit equation shown in (Erturk et al. 2010) for the case of a bi-morphed PZT beam with a resistor connected in parallel. The corresponding circuit diagram for Eq. (3) is shown in Figure 2 (b).

$$C_{eq}\dot{V} + \frac{V}{R} = \beta_f \dot{h} \tag{3},$$

where $C_{eq} = 2C_p$ is the equivalent capacitance; C_p is the capacitance of one PZT layer. R is the resistance.

In the numerical simulations, the flow induced lift and moment that form F_{fluid} in Eq. (1) are obtained by solving the unsteady Reynolds-averaged Navier-Stokes (uRANS) equation with a commercial CFD solver, ANSYS-CFX (2011). The flow is assumed to be 2-D, incompressible, and fully turbulent, and the κ–ω shear stress transport model is used as the turbulence model. To avoid numerical instability due to virtual added mass effect caused by the delay in exchange of surface traction and deformation between the fluid and solid solvers, the loose hybrid couple (LHC) method (Young et al. (2012), Chae et al. (2013), and Akcabay et al. (2014)) is used to couple the viscous flow solver and the solid model. However, contrary to the LHC method shown in Young et al. (2012), Chae et al. (2013), and Akcabay et al. (2014), only the potential flow approximation of the fluid added mass term is subtracted from both sides of the equation of motion; it has been shown in Akcabay et al. (2015) that addition of the fluid inertial term on both sides of the equation of motion is sufficient to stabilize the solution and accelerate convergence.

To derive similarity in response, the equations are non-dimensionalized with b for length, $\pi\rho_f b^2$ for mass per unit span, $2\pi/\omega_\theta$ for time, $\left[[\rho_f b^5 \omega_\theta^3/(8R\pi^2)\right]^{0.5}$ for current, $\left[\rho_f b^5 \omega_\theta^3 R/(8\pi^2)\right]^{0.5}$ for voltage, $2\pi/R\omega_\theta$ for capacitance, $\left[\rho_f b^3 \omega_\theta/(2R)\right]^{0.5}$ for electro-mechanical coupling coefficient, where ρ_f is the density of fluid. The discretized form of the non-dimensionalized versions of Eq. (1) and (3) can be written as follows:

$$\begin{aligned}&\left[\tilde{M}_s + \tilde{M}_f\right]\{\ddot{\tilde{X}}\}_n + \left[\tilde{C}_s\right]\{\dot{\tilde{X}}\}_n + \left[\tilde{K}_s\right]\{\tilde{X}\}_n \\ &= \{\tilde{F}_{fluid}\}_{n-1} + \{\tilde{F}_{PZT}\}_n + \left[\tilde{M}_f\right]\{\ddot{\tilde{X}}\}_{n-1}\end{aligned} \tag{4},$$

$$\tilde{C}_{eq}\dot{\tilde{V}}_n + \tilde{V}_n = \tilde{\beta}_f \ddot{\tilde{h}}_n \tag{5},$$

where,

$$\tilde{M}_s = \mu\begin{bmatrix} 1 & x_\theta \\ x_\theta & r_\theta^2 \end{bmatrix} \tag{6},$$

$$\tilde{M}_f = \begin{bmatrix} 1 & -a \\ -a & \frac{1}{8}+a^2 \end{bmatrix} \tag{7},$$

$$\tilde{C}_s = 2\pi\mu\begin{bmatrix} 2\Omega\zeta_{s,h} & 0 \\ 0 & 2r_\theta^2\zeta_{s,\theta} \end{bmatrix} \tag{8},$$

$$\tilde{K}_s = 4\pi^2\mu\begin{bmatrix} \Omega^2 & 0 \\ 0 & r_\theta^2 \end{bmatrix} \tag{9},$$

$$\tilde{F}_{PZT} = [4\pi^2/(b\omega_\theta^2)]\cdot\left[-V\beta_f/S_p \quad 0\right]^T \tag{10},$$

$$\tilde{F}_{fluid} = [4\pi^2/(b^2\omega_\theta^2)]\cdot\left[L_{fluid}b \quad M_{fluid}\right]^T \tag{11},$$

$\tilde{X} = [\ h/b \quad \theta\ ]^T$ is the non-dimensional displacement vector; $\tilde{M}_s$, $\tilde{C}_s$, $\tilde{K}_s$ are non-dimensional solid mass, damping, stiffness matrices; $\tilde{M}_f$ is the non-dimensional potential flow approximation of the fluid inertial matrix; $\tilde{F}_{PZT}$ is the non-dimensional PZT induced force/moment; $\tilde{F}_{fluid}$ is the non-dimensional flow induced force/moment; $\tilde{V} = V\left[\rho_f b^5 \omega_\theta^3 R/(8\pi^2)\right]^{-0.5}$ is the non-dimensional voltage; $\tilde{C}_{eq} = C_{eq}R\omega_\theta/(2\pi)$ is the non-dimensional capacitance;$\tilde{\beta}_f = \beta_f\left[\rho_f b^3 \omega_\theta/(2R)\right]^{-0.5}$; $\sqrt{\mu} = \sqrt{m/\pi\rho_f b^2}$ is the solid-to-fluid added mass ratio; $\Omega = (\omega_h/\omega_\theta)$ is the bending to twisting natural frequency ratio;

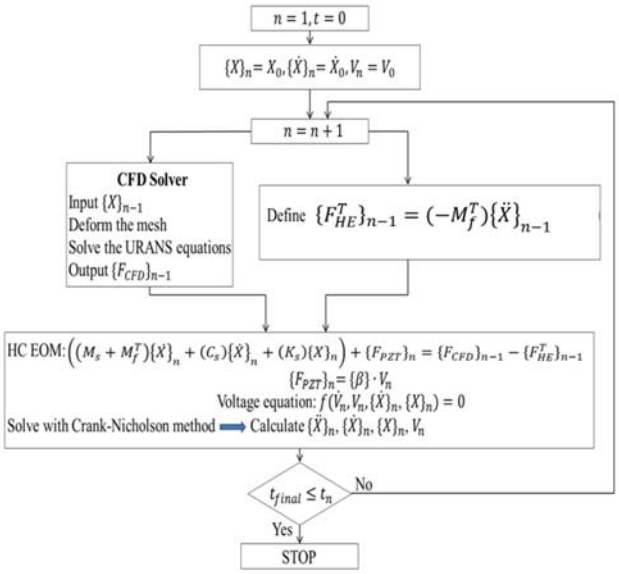

Figure 3: Flow chart showing the viscous LHC algorithm for the fluid, solid, and circuit equations.

Figure 3 shows the flow chart of the coupling between the fluid, solid, and circuit equation solvers. The equation of motion and electro-mechanical equations are solved using a semi-implicit Crank-Nicholson method to maintain second-order accuracy in time.

The numerical 2D NACA16-010 fluid mesh consists of approximately 76,000 elements and 48,000 nodes is shown in Figure 4. Unstructured triangular elements are used around foil surface except in the boundary layer region near the foil, which is discretized with the structured mesh. The mesh satisfies smallest element size with y^+=1 on the foil surface. To capture the flow details, the mesh is refined near the foil's leading and trailing edges, as well as in the wake region. The inlet uses prescribed constant inflow velocity (U), and 3% turbulence intensity with eddy length scale of 4.61×10^{-4}m. The outlet uses prescribed pressure boundary condition (P_0), and the foil surface uses no slip boundary conditions. The top, bottom, and domain surfaces used the symmetric boundary condition. The mesh elements are deformed according to the computed bending and twisting displacements of the hydrofoil at each time-step. The numerical simulations are initialized from the steady-state solution of the fluid flow around the foil with an initial twisting angle of $\theta_0 = -2°$ and initial bending deformation $h_0 = 0$.

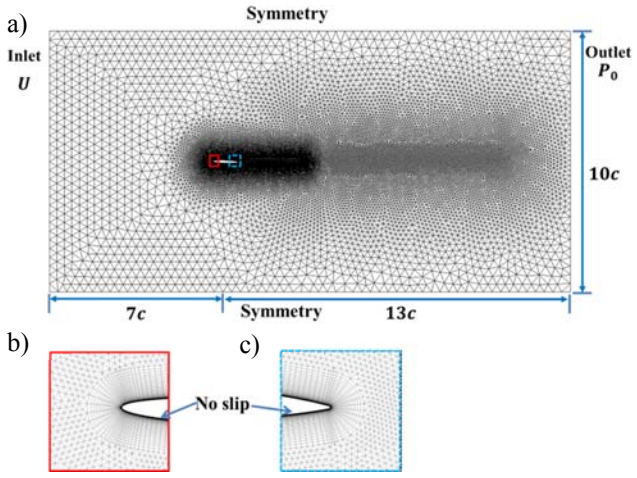

Figure 4: a) The 2D NACA16-010 mesh. b) Refined mesh at the leading edge. c) Refined mesh at the trailing edge. The rectangular domain size is $20c \times 10c$, where c is the chord length.

Detailed simulation parameters of the foil and fluid are shown in Table 1. To evaluate the control effect, PZT-5H is selected to be the PZT material used for the passive control method for its relative high electro-mechanical coupling effects compare to other PZT materials. The detailed parameters of the PZT-5H beam are shown in Table 2, where s_{11}^E is the elastic compliance at constant electric field; d_{31} is the piezoelectric constant; ε_{33}^T is the constant stress dielectric constant; ε_0 =8.854 [pF/m] is the permittivity of free space; $\bar{\varepsilon}_{33}^s = \varepsilon_{33}^T - d_{31}/s_{11}^E$ is the permittivity component at constant strain with the plane-stress assumption.

For the mesh deformation algorithm described in ANSYS (2011), the mesh elements are deformed to conform to the hydrofoil geometry according to the foil motions obtained by solving Eq. (4) and (5) using the LHC method at each time-step. Time and mesh convergence studies, as well as experimental validation studies of the LHC model for the same foil without PZT have already been presented in Chae et al. (2013), where good comparisons between the predicted and measured flutter and divergence speeds, and flutter frequencies were observed. In this work, we used the same mesh (approximately 76,000 elements and 48,000 nodes) and time step size of Δt=0.0004s as shown in Chae et al. (2013) to get converged solutions.

Table 1: Foil and Fluid Parameters

Parameter	Value
foil shape	NACA 16-010
foil material	Balsa wood
α_0 (initial angel of attack) [°]	0
a (non-dimensional distance between M.C. & E.A.) [-]	-0.218
x_θ (non-dimensional distance between E.A. & C.G.) [-]	0.068
Fluid	freon12/air mixture
S_p (span) [m]	1.2192
c (chord) [m]	0.3048
b (semi-chord) [m]	0.1524
E (Young's modulus) [Gpa]	1.8
$\zeta_{s,h}$ (solid damping of bending) [-]	0
$\zeta_{s,\theta}$ (solid damping of twisting) [-]	0
ν (poisson ratio) [-]	0.36
ρ_s (solid density) [kg/m^3]	97.2
ρ_s (fluid density) [kg/m^3]	2.2
μ_d (dynamic viscousity) [kg/(m·s)]	1.25×10^{-5}
τ/c (max thickness ratio)[-]	0.1
m (solid mass per unit span) [kg/m]	0.63
I_θ (solid inertial of moment per unit span) [kg·m]	2.4×10^{-3}
r_θ (non-dimensonal radius of gyration) [-]	0.4025
f_h (natural frequency of bending in vacuum) [Hz]	15.29
f_θ (natural frequency of twisting in vacuum) [Hz]	36.92
Ω (bending to twisting natural frequency ratio)[-]	0.41
$\sqrt{\mu}$ (solid-to-fluid added mass ratio) [-]	1.98

Table 2: PZT-5H Material Parameters

s_{11}^E [10^{-12} m^2/N]	16.5	$\bar{\varepsilon}_{33}^S$ [nF/m]	25.5
d_{31} [10^{-12} m/V]	-274	β_f [N/V]	3.74×10^{-2}
ε_{33}^T [ε_0]	3400	C_p [F]	3.83×10^{-7}

3 RESULTS AND DISCUSSION

Flutter control using PZT materials is the first step to analyze the passive control method. The dynamic response is evaluated by solving the coupled fluid, solid, and circuit equations in the time domain, as explained in Section 2. As mentioned earlier, comparisons of numerical predictions obtained using the viscous LHC method with experimental measurements from Woolston and Castile (1951) and Besch and Liu (1971) can be found in Chae et al. (2013) for airfoils and hydrofoils across a large range of solid-to-fluid added mass ratio $\sqrt{\mu} = \sqrt{m/\pi\rho_f b^2}$. For the sake of completeness, comparison of the predicted versus measured flutter and divergence speed, and with linear theory predictions, are shown in Figure 5. It should be noted that the flutter speed is found as the speed at which the total damping coefficient is zero. The total damping coefficient is evaluated by the logarithmic decrement method, which is explained in detail in Chae et al. (2013). Due to space limitations, only simulation results with and without PZT control for the case of $\sqrt{\mu} = 1.98$ (as marked by the red cross in Figure 5) are shown in the rest of this paper. For cases without PZT control, β_f in Eq. (3) is set to be zero, which means the PZT induced force is $F_{PZT} = 0$.

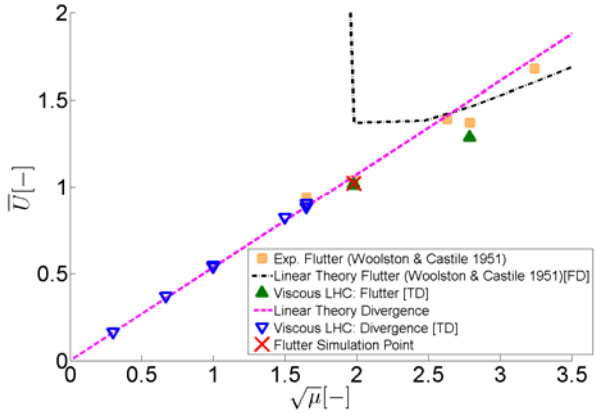

Figure 5: Static divergence and flutter velocity boundaries as a function of the solid to fluid added mass ratio. The pink and black dashed lines are the divergence boundary line and flutter boundary line calculated using linear theory. FD means a frequency domain method is used. The triangles are numerical results of divergence and flutter boundaries obtained using the viscous LHC method (Chae et al., 2013). TD means a time domain method is used. The squares are experimental results of flutter boundaries (Woolston and Castile, 1951). The flutter simulation point of focus in this work is shown as a red cross.

3.1 Flutter Boundary without PZT control

The results of the simulations without PZT control at $\sqrt{\mu} = 1.98$ very near the critical flutter point at $\overline{U} = U/2\pi f_\theta b = 1.02$, $Re = \rho_f Uc/\mu_d = 1.94\times10^6$ are shown in Figure 6. The time histories of bending deformation h, twisting

deformation θ, lift coefficient C_L, PZT force F_{PZT} and moment coefficient C_M of the predicted response without PZT control are plotted in red solid lines. The solid damping coefficients of bending ($\zeta_{s,h}$) and twisting ($\zeta_{s,\theta}$) are assumed to be both 0. Hence the fluid damping coefficient equals to the total damping coefficient, which is 0.03 as calculated using logarithmic decrement method.

3.2 Passive Flutter Control

To evaluate the effects of different passive PZT control methods, the same problem setup as described in Section 3.1 is used except that real PZT parameters as shown in Table 2 are used. The passive control circuit is now turned on at $\sqrt{\mu} = 1.98$, $\bar{U} = 1.02$, $Re = 1.94\times10^6$. As shown in the time histories of the deformations and load coefficients in Figure 6, activation of the PZT circuit increases the system damping, and hence helps to delay flutter. However, the effectiveness of the passive PZT circuit depends on the resistance (R). With $R = 10k\Omega$, the PZT passive control induces a larger damping term and works more effectively than the case with $R = 1k\Omega$.

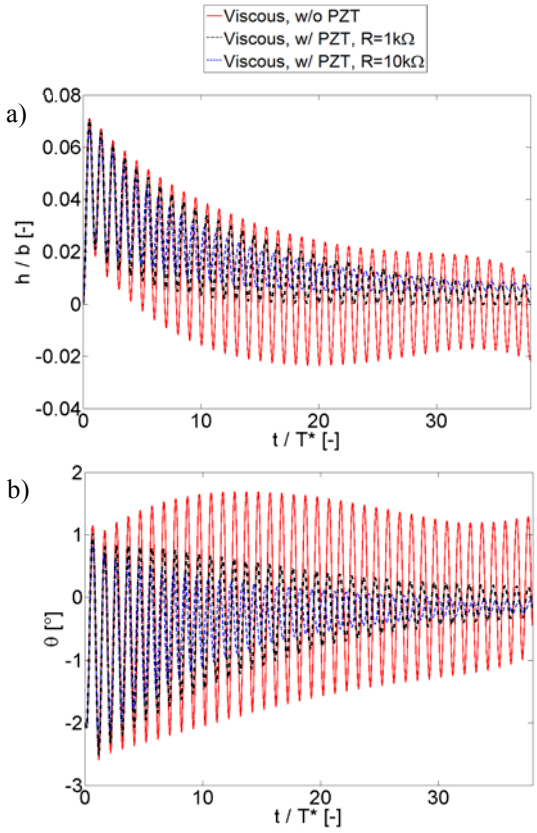

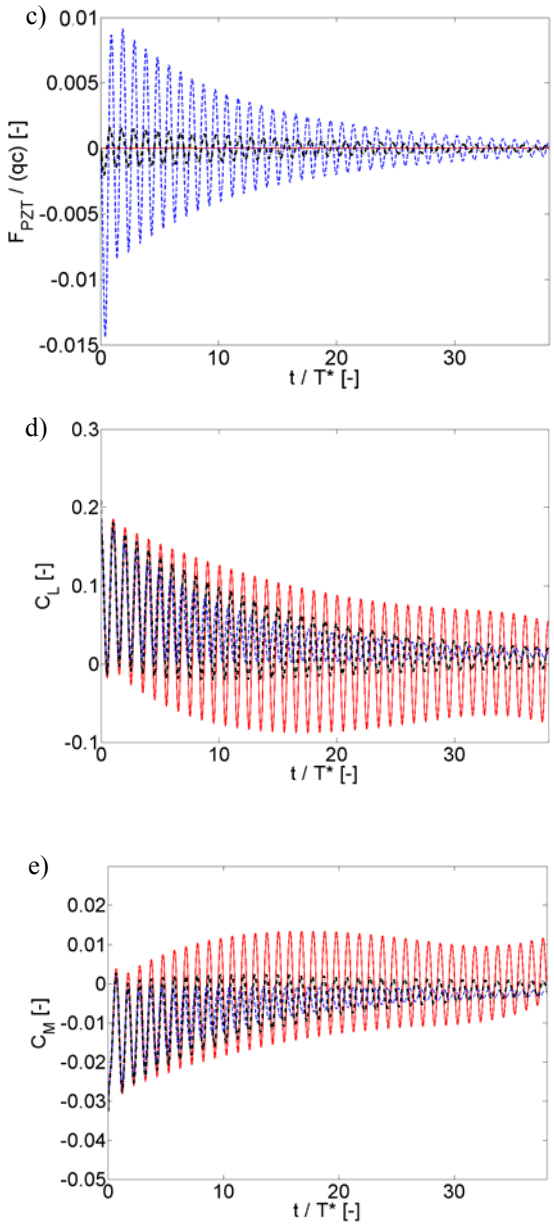

Figure 6: Time history comparisons of the a) bending deformation; b) twisting deformation; c) PZT force; d) lift coefficient; e) moment coefficient; without passive PZT control (red solid line), with passive PZT control for $R = 1k\Omega$ (black dot dashed line) and $R = 10k\Omega$ (blue dashed line), and at $\sqrt{\mu} = 1.98$, $\bar{U} = 1.02$, $Re = 1.94\times10^6$, with initial twisting angle of $\theta_0 = -2°$ and initial bending deformation $h_0 = 0$. $T^* = 1/f_{\theta-fluid}$. $f_{\theta-fluid}$ is the natural twisting frequency in the fluid. The forces are non-dimensionalized by qc, where $qc = 0.5\rho_f U^2 c$.

The non-dimensional vorticity patterns at selected time instances of the foil without PZT passive control method and with PZT control for $R = 1k\Omega$ and for $R = 10k\Omega$ at

$\sqrt{\mu} = 1.98$, $\bar{U} = 1.02$, $Re = 1.94\times10^6$ are shown in Table 3. The vorticity is non-dimensionalized by $\tilde{\varpi} = \varpi b/U$, where ϖ is the dimensional vorticity. The vorticity patterns of these three cases are similar, except that the vibrations get damped out faster with PZT for $R = 10k\Omega$.

Table 3: Vorticity Patterns Varying with Time

$\sqrt{\mu} = 1.98$, $\bar{U} = 1.02$, $Re = 1.94\times10^6$, with initial twisting angle of $\theta_0 = -2°$ and initial bending deformation $h_0 = 0$. $T^* = 1/f_{\theta-fluid}$. $f_{\theta-fluid}$ is the natural twisting frequency in the fluid.

without passive PZT control

with passive PZT control for $R = 1k\Omega$

with passive PZT control for $R = 10k\Omega$

$t = 1.5T^*$ $t = 15T^*$ $t = 30T^*$

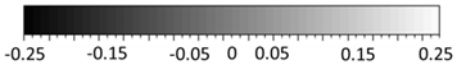

Non-dimensional vorticity $\tilde{\varpi} = \varpi b/U$

The frequency spectra of the bending and twisting deformations for the case without PZT, with PZT for $R = 1k\Omega$ and $R = 10k\Omega$ are shown in Figure 7. It should be noted that the frequency spectra of the lift and moment coefficients follow the same trends as the bending and twisting deformations, respectively, and hence they are not shown here. The vibration frequencies are normalized by natural twisting frequency in the fluid for the case without PZT ($f_{\theta-fluid}$). The results show the activation of the PZT circuit increases the vibration frequencies. For the case with PZT for $R = 10k\Omega$, the primary vibration frequency is at 1.025 $f_{\theta-fluid}$. For the case with PZT for $R = 1k\Omega$, the primary vibration frequency is at 1.001 $f_{\theta-fluid}$. The increase in the vibration frequency is due to the added stiffness caused by electro-mechanical coupling, which depends on the resistance. In Eq. (4), the force induced by PZT material could be divided into two components. One related to the bending motion at the current time step (h_n); the other related to the bending motion and voltage at the previous time step. Moving the term related to h_n to the stiffness matrix on the left hand side of Eq. (4) will show that the effective system stiffness will be increased by K_{PZT}, and hence the shifting of the frequency spectrum to the right, as shown in Figure 7. The increase in stiffness, K_{PZT}, is related to R. That is the reason that changing the resistance leads to the change of response frequency, which in turn changes the vibration amplitude.

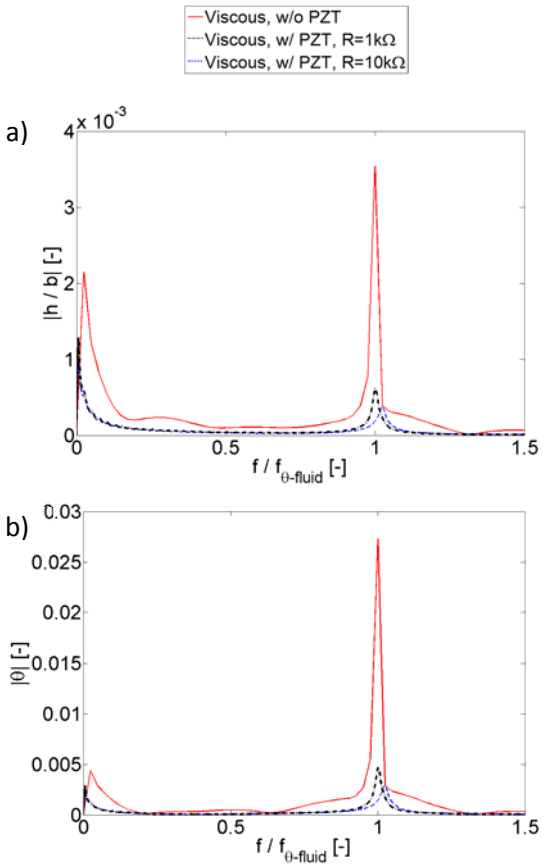

Figure 7: Frequency spectra of the a) bending motion; b) twisting motion; without passive PZT control (red solid line), with passive PZT control for $R = 1k\Omega$ (black dot dashed line) and $R = 10k\Omega$ (blue dashed line) at $\sqrt{\mu} = 1.98$, $\bar{U} = 1.02$, $Re = 1.94\times10^6$, with initial twisting angle of $\theta_0 = -2°$ and initial bending deformation $h_0 = 0$.

Figures 8 and 9 show phase plots of the non-dimensional voltage versus bending deformation, and non-dimensional PZT force versus lift coefficient with passive PZT control for $R = 10k\Omega$ and $R = 1k\Omega$, respectively.

The results show that for passive PZT control with $R = 1k\Omega$ and $R = 10k\Omega$, the trajectories of the voltage versus bending deformation and the trajectories of the PZT force versus lift, are spirals whose radius decrease along with time, i.e. the flow-induced vibrations and forces are decreasing with time. The spirals are mainly in the first and

fourth quadrants, which means the directions of PZT force and lift are switching between exactly in phase or exactly out of phase. In the first half of the total time (t_{hf}), the blue dashed line forms spirals. After t_{hf}, the spirals (red solid line) collapse to a point, which corresponds to steady-state values.

The voltage and PZT force change with the resistance. A higher resistance leads to a higher voltage and higher PZT force, and hence the different mean slope of the spirals shown in Figures 8 and 9.

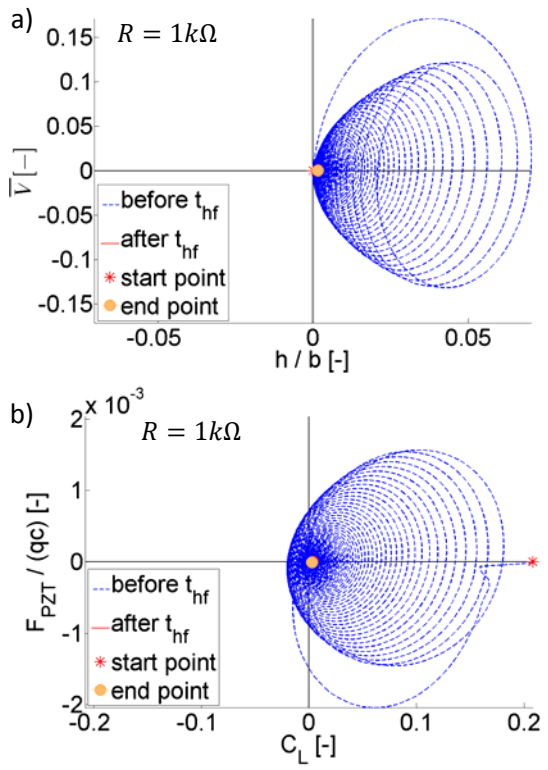

Figure 8: Phase plots (a) non-dimensional voltage $\bar{V} = V/\left[R\rho_f b^5\omega_\theta^3/(8\pi^2)\right]^{0.5}$ versus non-dimensional bending deformation (h/b), with passive PZT control for $R = 1k\Omega$; (b) non-dimensional PZT force $(F_{PZT}/(qc))$ versus lift coefficient (C_L), with passive PZT control $R = 1k\Omega$ at $\sqrt{\mu} = 1.98$, $\bar{U} = 1.02$, $Re = 1.94\times10^6$, with initial twisting angle of $\theta_0 = -2°$, $h_0 = 0$.The blue dashed line is the routine in the first half of the total simulation time (t_{hf}); the red solid line is the routine in the second half of the total simulation time; the red star is the start point and the orange solid circle is the end point.

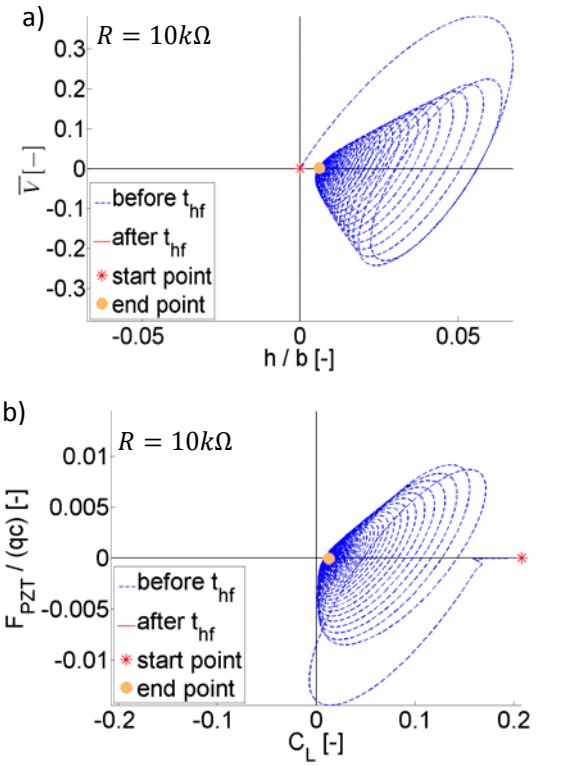

Figure 9: Phase plots (a) non-dimensional voltage $\bar{V} = V/\left[R\rho_f b^5\omega_\theta^3/(8\pi^2)\right]^{0.5}$ versus non-dimensional bending deformation (h/b), with passive PZT control for $R = 10k\Omega$; (b) non-dimensional PZT force $(F_{PZT}/(qc))$ versus lift coefficient (C_L), with passive PZT control for $R = 10k\Omega$ at $\sqrt{\mu} = 1.98$, $\bar{U} = 1.02$, $Re = 1.94\times10^6$, with initial twisting angle of $\theta_0 = -2°$, $h_0 = 0$. The blue dashed line is the routine in the first half of the total simulation time (t_{hf}); the red solid line is the routine in the second half of the total simulation time; the red star is the start point and the orange solid circle is the end point.

4 CONCLUSIONS AND FUTURE WORK

A bi-morphed PZT beam is coupled to the free-end of a cantilevered flexible foil as a passive flutter control method. The integrated fluid-solid-electrical response is modeled by coupling a 2-D viscous unsteady Reynolds Averaged Navier Stokes (uRANS) solver for the fluid with a two-degrees-of-freedom (2-DOF) solid model, which is coupled with the circuit equation. The two-way electro-mechanical coupling is assumed to be coupled to the foil bending degree of freedom only.

The results show that the damping effect of passive control method with PZT is dependent on the resistance. The resistance in the passive PZT control circuit adds an additional stiffness term to the total stiffness of the system. Hence, change of resistance lead to the change of vibration response. The magnitude of the voltage and the PZT induced force are also related to the resistance in the PZT control circuit.

The results suggest that a well-tuned resistor connected in parallel to the PZT material can help to delay flutter and control flow-induced vibrations.

The electro-mechanical model used in this work is a preliminary model. Additional research is being conducted to explore the change in response by connecting a resistor and an inductor in parallel, forming a LR shunted circuit to form a tuned vibration energy absorber. The current model only coupled the foil bending motion with electro-mechanical effect, which may make the control method not efficient in avoiding static divergence. For further investigation, the model will be modified by embedding PZT patches inside the foil and coupling the electro-mechanical effect with both bending and twisting deformations. Systematic studies are needed to examine the influence of the resistor, inductor, speed, and relative mass ratio on the effectiveness of using a PZT circuit for vibration control.

ACKNOWLEDGMENTS

The authors are grateful to the funding provided by Office of Naval Research (ONR) grant no. N00014-13-0383, managed by Dr. Ki-Han Kim.

REFERENCES

Akcabay, D. T., Chae, E. J., Young, Y. L., Ducoin, A., and Astol, A. (2014), "Cavity Induced Vibration of Flexible Hydrofoils," Journal of Fluids and Structures, 49, 463-484.

Akcabay, D. T., Xiao J., and Young, Y. L. (2015), "Numerical Stabilities of Loosely Coupled Methods for Robust Modeling of Lightweight and Flexible Structures in Incompressible and Viscous Flows," in preparation.

Ausoni, P. (2009), "Turbulent Vortex Shedding from a Blunt Trailing Edge Hydrofoil," PHD thesis, École Polytechnique Fédérale De Lausanne.

Bailey, T., and Ubbard, J. (1985), "Distributed Piezoelectric-Polymer Active Vibration Control of a Cantilever Beam," Journal of Guidance, Control, and Dynamics 8: 605-611.

Besch, P. K., and Liu, Y. (1971), "Flutter and Divergence Characteristics of Four Low Mass Ratio Hydrofoils," Tech. Rep. 3410, Naval Ship Research and Development Center.

Baz, A., and Poh, S. (1988), "Performance of an Active Control System with Piezoelectric Actuators," Journal of sound and Vibration 126: 327-343.

Blake, W. K., and Maga, L. J. (1975), "On the Flow−excited Vibrations of Cantilever Struts in Water. I. Flow−induced Damping and Vibration," The Journal of the Acoustical Society of America 57: 610-625.

Chae, E. J., Akcabay, D. T., and Young, Y. L., (2013), "Dynamic Response and Stability of a Flapping Foil in a Dense Viscous Fluid," Physics of Fluids, 25, 104-106.

Chae, E. J., Akcabay, D. T., Lelong, A., Astol, J., and Young, Y. L. (2015a), "Numerical and Experimental Studies on Flow-induced Vibrations of Flexible Hydrofoils," in preparation for Journal of Fluid and Structure.

Chae, E. J., Akcabay, D. T., and Young, Y. L. (2015b), "In Fluence of Flow-induced Bend-twist Coupling on the Dynamic Response, Wake structure, and Stability of Flexible hydrofoils," in preparation for Journal of Fluid and Structure.

Clark, W. W. (2000), "Vibration Control with State-Switched Piezoelectric Materials," Journal of Intelligent Material Systems and Structures 11: 263-271.

Corr, L.R., and Clark, W. W. (2002), "Comparison of Low-frequency Piezoelectric Switching Shunt Techniques for Structural Damping," Smart Materials and Structures 11: 370.

Doaré, O., and Michelin, S. (2011), "Piezoelectric Coupling in Energy-harvesting Fluttering Flexible Plates: Linear Stability Analysis and Conversion Efficiency," Journal of Fluids and Structures 27: 1357-1375.

Erturk, A., and Inman, D. J. (2009), "An Experimentally Validated Bimorph Cantilever Model for Piezoelectric Energy Harvesting from Base Excitations," Smart Materials and Structures 18: 025009.

Erturk, A., Vieira, W. G. R,, De Marqui, C., and Inman, D. J. (2010), "On the Energy Harvesting Potential of Piezoaeroelastic Systems," Applied Physics Letters 96: 184103.

Garrick, I. E. (1946), "Bending-torsion Flutter Calculations Modified by Subsonic Compressibility Corrections," Tech. Rep. 836, National Advisory Committee for Aeronautics.

Hagood, N. W., Chung, W. H., and von Flotow, A. (1990), "Modelling of Piezoelectric Actuator Dynamics for Active Structural Control," Journal of Intelligent Material Systems and Structures 1: 327-354.

Hagood, N. W., and Von Flotow, A. (1991), "Damping of Structural Vibrations with Piezoelectric Materials and Passive Electrical Networks," Journal of Sound and Vibration 146: 243-268.

Monner, H. (2005), "Smart Materials for Active Noise and Vibration Reduction", Proceedings of the Novem–Noise and Vibration: Emerging Methods, Saint-Raphael, France.

Reese, M. C. (2010), "Vibration and Damping of Hydrofoils in Uniform Flow," Phd thesis, The Pennsylvania State University.

Schwarzendahl, S. M., Szwedowicz, J., Neubauer, M., Panning, L., and Wallaschek, J. (2012), "On Blade Damping Technology Using Passive Piezoelectric Dampers," ASME Turbo Expo 2012: Turbine Technical Conference and Exposition, Copenhagen, Denmark.

Sears, W. R. (1941), "Some Aspects of Non-stationary Airfoil Theory and Its Practical Application," Journal of the Aeronautical Sciences (Institute of the Aeronautical Sciences) 8(3), 104-108.

Theodorsen, T. (1935), "General Theory of Aerodynamic Instability and the Mechanism of Flutter," Tech. Rep. 496, National Advisory Committee for Aeronautics.

Wu, S-Y. (1996), "Symposium on Smart Structures and Materials," International Society for Optics and Photonics, 259-269.

Wu, S-Y. (1998), "Method for Multiple Mode Piezoelectric Shunting with Single PZT Transducer for Vibration Control," Journal of Intelligent Material Systems and Structures 9: 991-998.

Young, Y. L., Chae, E. J., and Akcabay, D. T. (2012), "Hybrid Algorithm for Modeling of Fluid-structure Interaction in Incompressible, Viscous Flows," Acta Mech. Sin, 28(4), 1030-1041.